Research Article Vol. 12, No. 12 / 1 Dec 2022 / *Optical Materials Express* 4755

Optical Materials EXPRESS

Controlling localized states in a two-leg ladder lattice with diagonal edges via gain/loss [Invited]

RUI YE,[1] GUANGZHEN LI,[1,4] LUOJIA WANG,[1] XIAOXIONG WU,[1] LUQI YUAN,[1,*] AND XIANFENG CHEN[1,2,3]

[1] *State Key Laboratory of Advanced Optical Communication Systems and Networks, School of Physics and Astronomy, Shanghai Jiao Tong University, Shanghai 200240, China*
[2] *Shanghai Research Center for Quantum Sciences, Shanghai 201315, China*
[3] *Collaborative Innovation Center of Light Manipulation and Applications, Shandong Normal University, Jinan 250358, China*
[4] *liguangzhen520@sjtu.edu.cn*
[*] *yuanluqi@sjtu.edu.cn*

Abstract: Gain and loss engineering can bring fascinating physical phenomena and lead to useful potential applications in optics and photonics. Here we study a two-leg ladder lattice with diagonal-edge open boundary condition which supports zero-energy modes with localization phenomena. By considering the on-site gain and loss on two legs respectively, we see the phase transition of features from localization at edges to extension into bulk. Meanwhile, the effective magnetic flux can further enhance the localization effect. Simulations are performed to verify the manipulation of localization via gain and loss in our model. This work offers the opportunity for controlling the localized states in a finite system through the non-Hermiticity and shows potential application towards implementing high-power laser arrays in both real space and synthetic dimensions.

1. Introduction

Non-Hermitian physics has been widely studied to understand the property of various open systems [1–12]. Intriguing features including nonreciprocity [13–15], half-integer winding numbers [16,17], and non-Hermitian skin effect [18–22] are demonstrated both in non-Hermitian solid-state systems and photonics, which thus paves the way for potential applications, such as single-mode laser [23–25], sensitivity enhancement [26–28], and robust transmission of topological states [29–31]. In recent years, the parity and time reversal (PT) symmetry has attracted broad interest in non-Hermitian systems [3,32–35], since system can undergo phase transition between PT-unbroken and PT-broken phases, corresponding to real and complex energy spectra, respectively. Therefore, one can manipulate the topological properties of non-Hermitian system through PT symmetry and achieve exotic phenomena such as topological phase transition [36–38] and localized edge states [39–43]. For example, in photonics, the effect of PT symmetry on controlling the localized edge states has been widely studied in different platforms, where robust filed localization of topological edge state in finite PT-symmetric silicon waveguide [44], and controllable edge state localized at the interface by constructing a PT-symmetric Su-Schrieffer-Heeger model [45] have been observed. In many such studies, PT symmetry is introduced by gain and loss that are distributed in a geometrically symmetric way.

The bulk-boundary correspondence plays a fundamental role in the band theory of tight-binding models [46–52]. However, edge states that exhibits inside the band gap and is localized at the boundary are sensitive to the boundary condition [53–55]. Therefore, one can control the behavior of edge states by designing different boundary conditions [56,57]. In addition, the

#477926 https://doi.org/10.1364/OME.477926
Journal © 2022 Received 10 Oct 2022; revised 12 Nov 2022; accepted 14 Nov 2022; published 1 Dec 2022

ladder system has been proven to be a powerful platform for characterizing edge states, due to its simple geometry, abundant phase diagrams and diverse types of boundaries [58–63]. Rich behaviors of edge states have been obtained by manipulating the type of boundaries in ladder systems, for example, achieving topological trivial and nontrivial edge states in vertical edge and diagonal edge open boundary conditions [64]. In addition, non-Hermiticity is also been introduced into the ladder system, where interesting physics such as topological transformation of the non-Hermitian skin effect and dynamical signature of the moiré pattern are explored [65,66]

In this work, we study a finite two-leg ladder model with on-site gain and loss on two legs respectively, and study the behavior of localized states, which can be controlled by the amplitude of gain/loss. As aforementioned, non-Hermitian system is highly sensitive to boundary conditions. Different from the condition in periodic boundary condition (PBC), which clearly exhibits an exceptional point (a non-Hermitian degeneracy) [67], here we investigate the two-leg ladder model in the diagonal-edge open boundary condition (OBC) [64,68] together with on-site gain and loss and effective magnetic flux. We find that the complex eigenvalues of the lattice can still be manipulated by both the amplitude of gain/loss γ and also the influence of the effective magnetic flux ϕ. In particular, we see that when γ is small, the localized edge states exist, which holds pure gain or loss at different edges. However, when γ becomes larger, the eigen-modes of the lattice all extend into the bulk of the lattice. Different from previous works on non-Hermitian lattices with edge states [57,69–71], our study shows features of localizations in a ladder lattice with the diagonal-edge OBC and the effects of the transition from localization at edges to extension into bulk in the fluence of the gain/loss non-Hermicity and the effective magnetic flux, which could be useful for manipulating the edge-mode lasing in both real space and synthetic dimensions.

2. Model

We begin with considering a two-leg ladder model formed by leg A and leg B under periodic boundary condition as shown in Fig. 1(a), where the lattice sites are labelled as A_n (red circle) and B_n (blue circle), respectively. Sites A_n and B_n at the same n are coupled at a longitudinal coupling strength w. The horizontal nearest-neighbor sites in leg A and leg B are connected by asymmetric couplings with $V_a e^{\pm i\phi_a}$ and $V_b e^{\pm i\phi_b}$, respectively. V_a, V_b and ϕ_a, ϕ_b are the corresponding coupling amplitudes and phases. Such configuration can induce an effective magnetic flux represented by $\phi = \phi_a - \phi_b$ [72]. On-site gain and loss are also applied on leg A and leg B with the same values γ, which can introduce non-Hermiticity into the two-leg ladder system. Then one can obtain the Hamiltonian of the system as

$$H = \sum_n \left[i\gamma\left(a_n^\dagger a_n - b_n^\dagger b_n\right) + w(a_n^\dagger b_n + b_n^\dagger a_n) + V_a e^{-i\phi_a} a_n^\dagger a_{n+1} + V_b e^{-i\phi_b} b_n^\dagger b_{n+1} + h.c.\right], \tag{1}$$

where $a_n^\dagger$ and $b_n^\dagger$ (a_n and b_n) are the creation (annihilation) operators for lattice sites A_n and B_n, respectively. We can further transfer Eq. (1) into the momentum space (k space)

$$H' = i\gamma\left(a_k^\dagger a_k - b_k^\dagger b_k\right) + w\left(a_k^\dagger b_k + b_k^\dagger a_k\right) + 2V_a \cos\left(k + \phi_a\right) a_k^\dagger a_k + 2V_b \cos\left(k + \phi_b\right) b_k^\dagger b_k. \tag{2}$$

The corresponding Bloch Hamiltonian of the system reads

$$H_k = \begin{pmatrix} 2V_a \cos(k + \phi_a) + i\gamma & w \\ w & 2V_b \cos(k + \phi_b) - i\gamma \end{pmatrix}, \tag{3}$$

which satisfies $\boldsymbol{PT} H_k \boldsymbol{PT}^{-1} = H_k$ under conditions $V_a = V_b$ and $\phi_a = \phi_b$. Here $\boldsymbol{P}$ and $\boldsymbol{T}$ represent the parity and time reversal operators, respectively. The corresponding eigenvalues of the system in Fig. 1(a) are

$$E_{\pm} = V[\cos(k+\phi_a) + \cos(k+\phi_b)] \pm \sqrt{[V\cos(k+\phi_a) - V\cos(k+\phi_b) + 2i\gamma]^2 + 4w^2}, \qquad (4)$$

where we set $V_a = V_b = V$ for simplicity. When there is no phase difference, i.e. $\phi_a = \phi_b = 0$, the eigenvalues in Eq. (4) turns into a well-known form $E_{\pm} = 2V\cos(k) \pm 2\sqrt{w^2-\gamma^2}$ [73]. We take $V = 0.2, w = 0.5$ and plot the real and imaginary parts of the eigenvalues [Re(E) and Im(E)] at $k = 0$ described by Eq. (4) as a function of γ in Fig. 1(b) with $\phi_a = \phi_b = \pi/2$. Note that parameters V, w, and γ have the same unit as the energy and we assume them unitless for the simplicity. The model is then scalable. One sees that the system has real eigenvalues without imaginary parts (PT-unbroken phase) when $\gamma<w$, which becomes complex ones once $\gamma>w$ (PT-broken phase). The real and imaginary parts of the eigenvalues degenerate to one point at $\gamma = w$. This bifurcation point, also known as the exceptional point (EP), corresponds to the PT unbroken-broken threshold, which is the key feature of non-Hermitian systems [74].

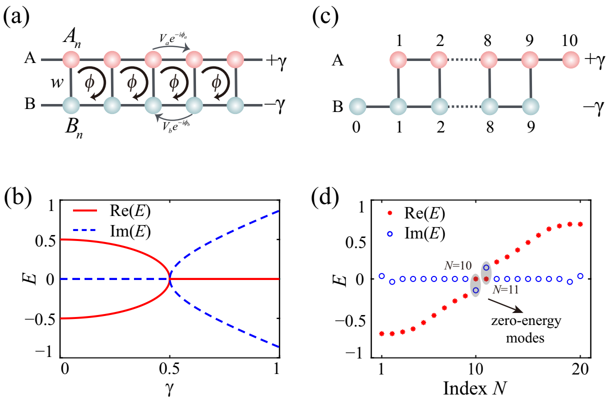

Fig. 1. (a) Schematic of a periodic two-leg ladder system with on-site gain ($+\gamma$) and loss ($-\gamma$) applied on leg A and leg B, respectively. (b) The energy spectrum of the system in (a) as a function of the on-site gain and loss γ with $V = 0.2, w = 0.5$, and $\phi_a = \phi_b = \pi/2$ at $k = 0$. (c) A finite two-leg ladder system with on-site gain and loss γ under the diagonal-edge boundary condition. (d) The eigenvalues of the lattice model in (c) with $V = 0.2, w = 0.5, \gamma = 0.2$, and $\phi = 0$. The bottom horizontal axis represents the number index (N) of the eigenvalue.

On the basis of Fig. 1(a), we consider a finite two-lag ladder system under open boundary condition with total sites number $2n = 20$ as shown in Fig. 1(c), where both legs contain 10 lattice sites labelled as $A_m (m = 1, 2 \cdots 10)$ and $B_j (j = 0, 1 \cdots 9)$, respectively. Site A_{10} and site B_0 have no longitudinal coupling, which thus constructs a diagonal edge configuration on this lattice model. Due to the finite lattice structure, k therefore is no longer a good quantum number. One can calculate the corresponding energy spectrum (E_N) by diagonalizing the Hamiltonian in Eq. (1) with 2×10 lattice sites, which is plotted in Fig. 1(d) under the regime with $\gamma<w$, where one sees a pair of eigenstates (called zero-energy modes) located at the real energy gap ($N = 10$ and $N = 11$). Here, $N = 1, 2 \cdots 20$ stands for the number of the eigenvalues. The two zero-energy modes have zero real eigenvalues but conjugate imaginary parts, which indicates the existence of edge states [69]. However, for a different boundary condition such as a vertical-edge OBC, there is no zero-energy mode and hence the corresponding localized edge states do not exist. In the following, we will show the effects of on-site gain and loss γ as well as the effective magnetic flux ϕ in the finite two-leg ladder system with the diagonal-edge OBC.

3. Theoretical analysis

We first explore the effect of the on-site gain and loss γ in the lattice with the diagonal edge shown in Fig. 1(c) with $\phi = 0$ and $V = 0.2$, and calculate the energy spectra with varied longitudinal coupling strength w, which are plotted in Fig. 2. For the special case $w = 0$, the two legs of the ladder lattice become independent, in which case the system does not support zero-energy mode since the system is always under the regime with $\gamma > w$ [see Fig. 2(a)]. When the longitudinal coupling w is included [see Figs. 2(b)-(d)], the system experiences phase transition at $\gamma = w$. The two branches in the imaginary part of eigenvalues correspond to the zero-energy modes in the real part. As we will show next that the zero-energy modes manifest at the regime with $\gamma < w$ and disappear at the regime with $\gamma > w$, which shows a transition that is linked to the PT transition in an infinite model.

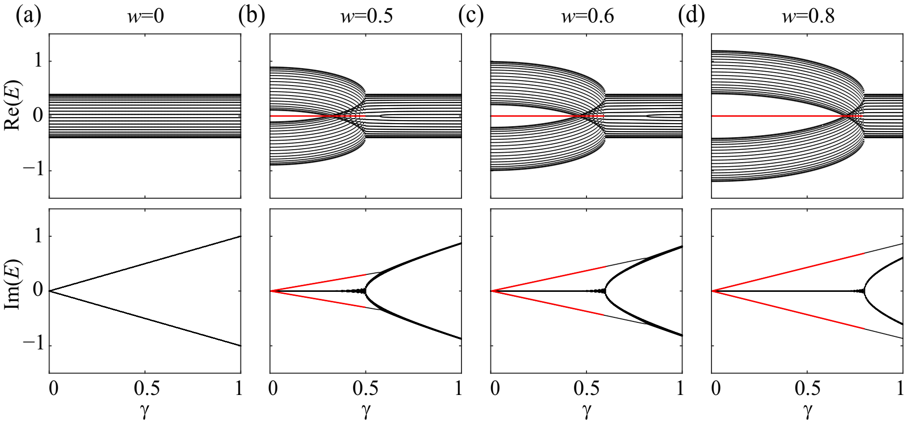

Fig. 2. The energy spectra of the lattice model as a function of on-site gain and loss γ under conditions (a) $w = 0$, (b) $w = 0.5$, (c) $w = 0.6$, and (d) $w = 0.8$, with $V = 0.2$ and $\phi = 0$. The upper and lower panels denote the real and imaginary parts of the eigenvalues solved from Eq. (1), respectively. Red lines correspond to zero-energy modes.

To unveil the nderlyings of the non-Hermiticity, we focus on studying the properties of the zero-energy modes. Let ψ_N be the eigenstate corresponding to the N^{th} eigenvalue (E_N) of the Hamiltonian in Eq. (1), which satisfies the Schrödinger equation $H\psi_N = E_N\psi_N$. For a specific eigenvalue E_N, the projection of the eigenstate on each lattice site is defined as $\psi_N = (\psi_{A,m}, \psi_{B,j})^{\mathrm{T}}$, where $\psi_{A,m}(m = 1, 2 \cdots 10)$ and $\psi_{B,j}(j = 0, 1 \cdots 9)$ are the projections on the lattice sites in leg A and leg B, respectively. We only consider the eigenstates corresponding to the two eigenvalues E_{10} and E_{11} [see Fig. 1(d)], whose intensity distributions are plotted in Figs. 3(b1)-(c3) with choices of $w = 0.5$ and $\gamma = 0, 0.4, 0.8$, respectively. The upper and lower panels in each subfigure of Figs. 3(b1)-(c3) show the intensity projections of the eigenstates $\left|\psi_{A,m}\right|^2$ (red bars) and $\left|\psi_{B,j}\right|^2$ (blue bars), respectively. First, we consider a conventional two-leg ladder system without on-site gain and loss ($\gamma = 0$) [see Figs. 3(b1)-(c1)], under which condition the real and imaginary parts of the two eigenvalues E_{10} and E_{11} are both close to zero [see Fig. 3(a1)]. One notes that for the eigenvalue E_{10} with negative imaginary part, the energy of the eigenstate mainly distributes on lattice site B_0 [see Fig. 3(b1)], namely, on the edge of leg B, while the energy mainly distributes on the edge of leg A (site A_{10}) [see Fig. 3(c1)] for the eigenvalue E_{11} with positive imaginary part. It means that this hermite two-leg ladder system naturally supports the existence of edge states that localizes at the edge (also called localized edge state). When the on-site gain and loss γ is applied, one sees that the localized edge states still hold under the condition of $\gamma = 0.4 < w$, but with a little attenuation of the localization effect [see Figs. 3(b2)-(c2)]. The localization of the eigenstate collapses when the system experiences larger γ, i.e., $\gamma = 0.8 > w$ here, while the real parts of the E_{10} and E_{11} are no longer close to zero. In this case, there is no edge state supporting the localization feature, but interestingly, the eigenstates of E_{10} and E_{11} have nearly uniform distributions only on leg B [see Figs. 3(b3)] or leg A [see Figs. 3(c3)], respectively.

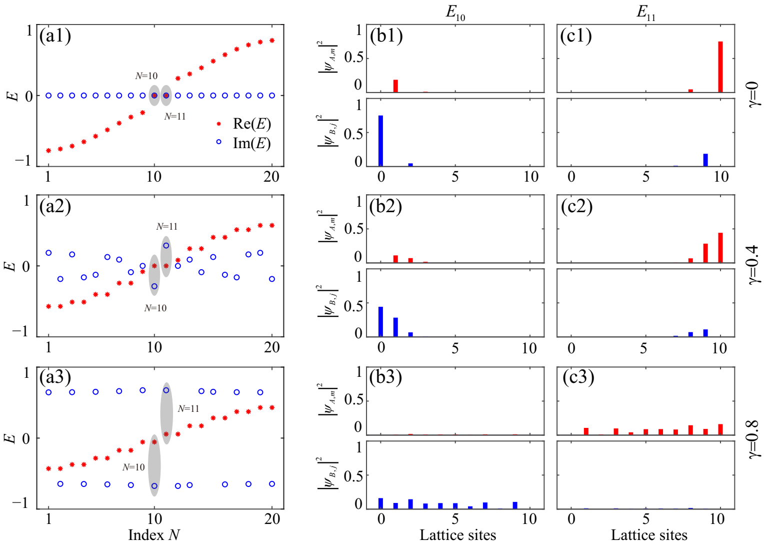

Fig. 3. Energy spectra and intensity distributions for the localized edge states on a $2n = 20$ two-leg ladder with $w = 0.5, \phi = 0.5\pi$. (a1)-(a3) Energy spectra, and (b1)-(c3) Intensity distribution of the eigenstates of E_{10} and E_{11}, for different $\gamma = 0, 0.4, 0.8$, respectively.

In order to further characterize the localization effect of the eigenstates, we define the inverse participation ratio (IPR) for the zero-energy modes E_{10} and E_{11} as [75]

$$\mathrm{IPR} = \frac{\sum_m |\psi_{A,m}|^4 + \sum_j |\psi_{B,j}|^4}{\left(\sum_m |\psi_{A,m}|^2 + \sum_j |\psi_{B,j}|^2\right)^2}, \tag{5}$$

and plot it in Fig. 4 for different values of w that corresponds to Fig. 2. There is no localization effect when $w = 0$ (IPR=0.136) due to the independence of the two legs. Once w is added, the localization effect shows up at the regime with $\gamma < w$ and disappears at the regime with $\gamma > w$. One also sees that the strength of the localization is maximum at $\gamma = 0$, and decreases as γ increases when $\gamma < w$.

We further study the influence of effective magnetic flux ϕ on this two-leg ladder lattice in Fig. 1(c). We plot the energy spectra of the system varied with ϕ for different values of on-site gain and loss γ while keeping $V = 0.2$ and $w = 0.5$ in Fig. 5. Without gain and loss ($\gamma = 0$), the system becomes Hermitian, where real eigenvalues are seen in Fig. 5(a). The zero-energy modes locate at the real energy gap through the entire effective magnetic flux interval [$\phi \in (0, 2\pi)$]. When the on-site gain and loss is added, the eigenvalues become complex [see Figs. 5(b)-(d)]. The real energy gap only opens up within a certain range of ϕ if the system stays in the regime with $\gamma < w$, where the existence of the zero-energy modes still holds through the entire range of ϕ $(0, 2\pi)$ [see Fig. 5(b)]. The real energy gap closes up if the system turns becomes $\gamma > w$, which does not support the zero-energy mode any more [see Fig. 5(d)].

We exhibit the effect the effective magnetic flux ϕ on the distributions of the eigenstates that corresponds to the zero-energy modes following the same procedure of Fig. 3, which are shown in Figs. 6(a)-(f) with the system at the condition of $\gamma = 0.4, w = 0.5$. We also plot the distributions

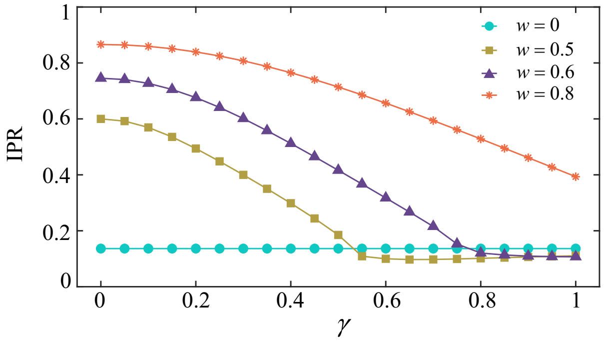

Fig. 4. Inverse participation ratio (IPR) of zero-energy modes versus gain and loss coefficient γ for the various w.

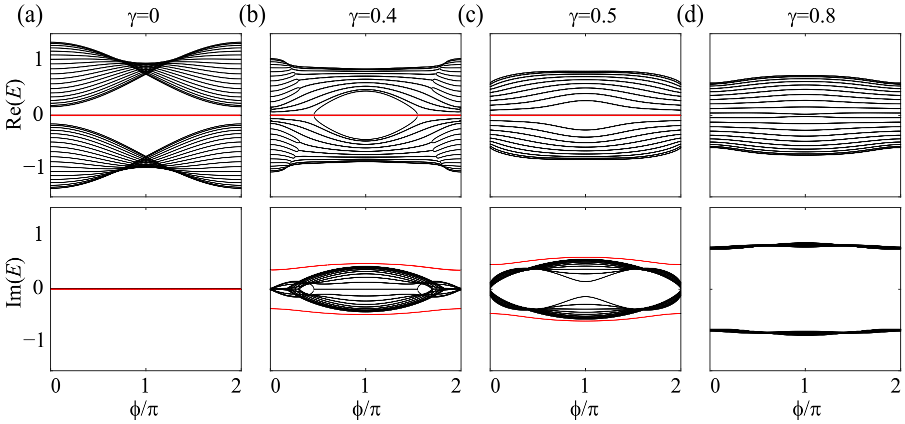

Fig. 5. The energy spectra in Fig. 1(c) as a function of the effective magnetic flux ϕ under (a) $\gamma = 0$, (b) $\gamma = 0.4$, (c) $\gamma = 0.5$, (d) $\gamma = 0.8$, with parameters $V = 0.2$ and $w = 0.5$. The upper and lower panels denote the real and imaginary parts of the eigenvalues, respectively. Red lines correspond to zero-energy modes.

of the eigenstats on the lattice sites in leg A ($\left|\psi_{A,m}\right|^2$) and leg B ($\left|\psi_{B,j}\right|^2$) separately in the upper and lower panels of each subfigure in Figs. 6(a)-(f). Without the effective magnetic flux ($\phi = 0$), only less than half of energy of the eigenvalues distribute on the edge of leg B [see Fig. 6(a)] or leg A [see Fig. 6(b)], which is decided by the sign of imaginary part of the eigenvalues. Meanwhile, the rest of the energy scatters into the bulk [see Fig. 6(a)-(b)]. The localization effect becomes stronger if ϕ falls in the real energy gap [see Fig. 5(b) and Figs. 6(c)-(f)], which reaches to the maximum when $\phi = \pi$ [see Figs. 6(e)-(f)]. Similarly, we plot the corresponding IPR as a function of ϕ when γ varies in Fig. 6(g). Without on-site gain and loss ($\gamma = 0$), the system has the strongest localization effect. In certain range of ϕ, the localization effect increases along with ϕ if the system stays at the regime with $\gamma<w$, which approaches to the maximum IPR at $\phi = \pi$. We also see that ϕ has no effect on the localization if γ exceeds the threshold with $\gamma = w$ ($\gamma = 0.8$).

One can clearly see that both the on-site gain and loss γ as well as the effective magnetic flux ϕ have the capability to control the localized edge state of the non-Hermitian two-leg ladder system with the diagonal edge. Here, we exhibit the interplay between the two factors on the IPR and show the phase diagram in the case of $V = 0.2$ and $w = 0.5$ in Fig. 7. The larger IPR with smaller γ and larger ϕ (up to π) could be the result from larger size of band gap, as one can

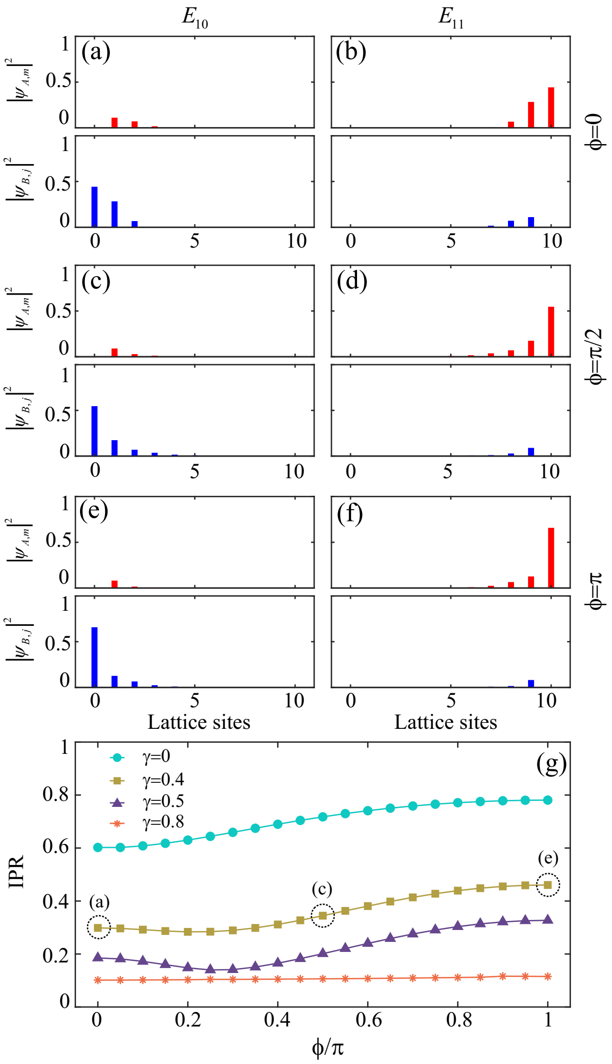

Fig. 6. Intensity distributions for the localized edge states with $w = 0.5, \gamma = 0.4$. (a)-(f) Intensity distribution of the eigenstats of E_{10} and E_{11} for different values of ϕ, (a)-(b) $\phi = 0$, (c)-(d) $\phi = \pi/2$, (e)-(f) $\phi = \pi$. (g) IPR of zero-energy modes versus gain and loss coefficient γ for the various ϕ.

see from both Figs. 2 and 5. The zero-energy mode has the maximum IPR at $\gamma = 0$ and $\phi = \pi$. When γ becomes larger, IPR decreases for each choice of ϕ. Nevertheless, if we define a critical value of IPR = 0.185, which corresponds to the IPR value under the choice of $\gamma = 0.5$ and $\phi = 0$, one can see that the transition of IPR is pushed toward higher value of γ when larger effective magnetic flux is introduced (i.e., ϕ approaches approximately larger than $\pi/2$).

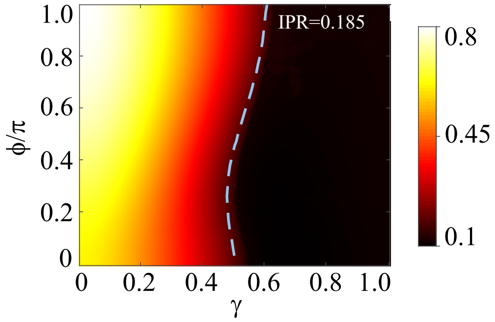

Fig. 7. Phase diagram of the IPR as a function of on-site gain and loss (γ) and the effective magnetic flux (ϕ). Dashed blue line indicates the contour line of IPR = 0.185, which corresponds to the IPR value under the choice of $\gamma = 0.5$ and $\phi = 0$.

4. Numerical simulations

We perform the numerical simulations to verify the properties of the studied localization effects in this two-leg ladder system in Fig. 1(c) with the input excitation. We define the wave function of light as

$$|\varphi(t)\rangle = \left[\sum_{m=1}^{10} v_{a,m}(t)\, a_m^\dagger + \sum_{j=0}^{9} v_{b,j}(t)\, b_j^\dagger\right] |0\rangle\,, \tag{6}$$

where $v_{a,m}$ and $v_{b,j}$ represent the amplitude of the photon states at lattice sites A_m and B_j, respectively. By solving the Schrödinger equation $i\frac{d}{dt}|\varphi\rangle = H|\varphi\rangle$ with H defined by Eq. (1), one obtains the coupled mode equations

$$\begin{aligned} \dot{v}_{a,m}(t) &= \gamma v_{a,m}(t) - iwv_{b,j}(t) - iV\left(v_{a,m+1}e^{-i\phi_a} + v_{a,m-1}e^{i\phi_a}\right) + iS_{\text{in}}\delta_{m,m'}, \\ \dot{v}_{b,j}(t) &= -\gamma v_{b,j}(t) - iwv_{a,m}(t) - iV\left(v_{b,j+1}e^{-i\phi_b} + v_{b,j-1}e^{i\phi_b}\right) + iS_{\text{in}}\delta_{j,j'}. \end{aligned} \tag{7}$$

Here S_{in} refers to the input pulse shape that excites a particular site m' or j'.

In simulations, we continue work with unitless parameters and keep $V = 0.2$ and $w = 0.5$. The input source with a Gaussian shape is used, i.e., $S_{\text{in}} = e^{-(t-25)^2/100}$. We first study the case without gain and loss γ ($\gamma = 0$) and $\phi = \pi/2$ [see Figs. 8(a1)-(c1)], which corresponding to the energy spectrum in Fig. 3(a1). The lattice is a normal system and the energy spectrum is real. We find that the consequence of steady-state result in simulation is sensitive to the location of excitation (as shown by the red arrow). We excite at the two endpoints ($m' = 10$ on leg A and $j' = 0$ on leg B, respectively) and take $t = 100$ so the simulation reaches a steady state. The corresponding simulation results are plotted in Figs. 8(a1)-(b1), where one can see that the energy is eventually localized at the excitation site in both simulations. However, if we excite at the middle site ($m' = 6$ on the leg A) as shown in Fig. 8(c1), the result shows the energy of light is distributed all over lattice sites. In this simulation, the bulk state is excited. Moreover, the total

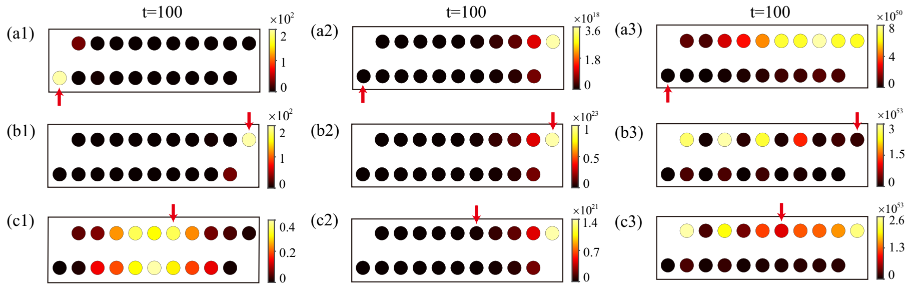

Fig. 8. Simulation results of intensity distributions the ladder model in Fig. 1(c) with parameters $V = 0.2, w = 0.5, \phi = 0.5\pi$ and different γ. (a1)-(c1) $\gamma = 0$, (a2)-(c2) $\gamma = 0.4$, (a3)-(c3) $\gamma = 0.8$.

energy excited in the lattice is much smaller than those in previous two simulations, due to the fact that the off-resonant excitation to the bulk mode in this case.

We next consider the non-Hermitian case with the choice of $\gamma = 0.4, \phi = 0.5\pi$, which corresponds to the energy spectrum shown in Fig. 3(a2). In this case, it exhibits two zero-energy modes with opposite imaginary parts, where only the one supporting the localized mode at $m = 10$ in the A leg has the gain. We again excite the lattice using the same input excitations at three different sites as those in the previous set of simulations and show the results in Figs. 8(a2)-(c2). We find that in all three cases, a lasing behavior at the top right edge in the lattice exhibits, no matter whether the system is excited at the bottom left edge or at the middle site. The reason is that the zero-energy mode with the positive imaginary part of the eigen-energy has the maximum gain over all other modes, and hence can eventually increase fast in intensity in a long time scale. The results also show that it is indeed the case that we excite at the top right edge [Fig. 8(b2)] gathering the most energy in the localized edge state among three cases. A high IPR = 0.3446 is found in this case.

Lastly, we consider the simulations with $\gamma = 0.8$, corresponding to the energy spectrum in Fig. 3(a3). There is no edge mode exiting, and all modes show the bulk distribution feature. However, one notices that only sites on leg A experience the gain. Therefore, in simulations with three different inputs, we see extended distributions on leg A, which accumulate with spatial fluctuation versus time.

5. Discussion and conclusion

Our proposed lattice model is potentially feasible on various experimental platforms. The development of integrated technology paves the way for the realization of coupled resonator models, such as integrated microring resonator arrays that exhibits edge-mode lasing [76–78], and photonic waveguide arrays supporting topological edge states [45,79]. In particular, coupled microrings with silicon or lithium niobite photonic technologies [78,80–83] have shown the great capability for simulate physics associated with tight-binding models. In such designs, one can use auxiliary asymmetric waveguides to couples microrings in order to introduce the effective magnetic flux [80]. The non-Hermicity can be introduced by either unbalanced loss engineering with a global loss offset or adding active optical gain [3]. On the other hand, in addition to the real space, one can construct the effective artificial lattice structure in synthetic dimension [84]. Particularly, in photonics, it offers a rich set of physical states for constructing synthetic lattices. For example, one can create the proposed model by coupling different frequency modes in two rings where one experiences gain and the other one has loss [85–89]. In this case, modulation phases can introduce the effective magnetic flux [84]. Moreover, by adding additional small rings, one can arbitrary knock off a particular frequency mode in this synthetic frequency lattice

[90], and hence constructs the diagonal-edge OBC. Alternatively, one can utilize the temporal degree of freedom and build the time-multiplexed lattice model with multiple pulses [91–94].

In summary, we provide a detailed study of a two-leg ladder lattice with the diagonal-edge OBC with additional gain and loss applied on two legs respectively. We find that, with small gain and loss, the system holds a pair of zero-energy modes with pure positive and negative imaginary eigenvalues that exhibit localized distributions at edges. When the gain and loss further increase, a phase transition happens and the localization features collapse. Moreover, the introduction of the effective magnetic flux can influence the localization effect and then result in the larger IPR. Simulations results present phenomena consistent to the theoretical analysis, and interestingly, we show the existence of the gain mode localized at the edge. Our work offers the opportunity for manipulating edge states with pure gain or loss in such lattice model and could finds potential applications in achieving high-power laser arrays.

Funding. National Natural Science Foundation of China (11974245, 12104297, 12122407, 12192252, 12204304); Shanghai Municipal Science and Technology Major Project (2019SHZDZX01-ZX06).

Acknowledgments. L.Y. thanks the sponsorship from Yangyang Development Fund and the support from the Program for Professor of Special Appointment (Eastern Scholar) at Shanghai Institutions of Higher Learning.

Disclosures. The authors declare no conflicts of interest.

Data availability. Data underlying the results presented in this paper are not publicly available at this time but may be obtained from the authors upon reasonable request.

References

1. Y. Ashida, Z. Gong, and M. Ueda, "Non-Hermitian physics," Adv. Phys. **69**(3), 249–435 (2020).
2. H. Wang, X. Zhang, J. Hua, D. Lei, M. Lu, and Y. Chen, "Topological physics of non-Hermitian optics and photonics: a review," J. Opt. **23**(12), 123001 (2021).
3. L. Feng, R. El-Ganainy, and L. Ge, "Non-Hermitian photonics based on parity–time symmetry," Nat. Photonics **11**(12), 752–762 (2017).
4. B. Midya, H. Zhao, and L. Feng, "Non-Hermitian photonics promises exceptional topology of light," Nat. Commun. **9**(1), 2674 (2018).
5. S. Longhi, "Parity-time symmetry meets photonics: a new twist in non-Hermitian optics," Europhys. Lett. **120**(6), 64001 (2017).
6. W. Zhang, X. Ouyang, X. Huang, X. Wang, H. Zhang, Y. Yu, X. Chang, Y. Liu, D.-L. Deng, and L.-M. Duan, "Observation of non-Hermitian topology with nonunitary dynamics of solid-state spins," Phys. Rev. Lett. **127**(9), 090501 (2021).
7. T. Liu, Y.-R. Zhang, Q. Ai, Z. Gong, K. Kawabata, M. Ueda, and F. Nori, "Second-order topological phases in non-Hermitian systems," Phys. Rev. Lett. **122**(7), 076801 (2019).
8. P. A. McClarty and J. G. Rau, "Non-Hermitian topology of spontaneous magnon decay," Phys. Rev. B **100**(10), 100405 (2019).
9. T. Yoshida, R. Peters, and N. Kawakami, "Non-Hermitian perspective of the band structure in heavy-fermion systems," Phys. Rev. B **98**(3), 035141 (2018).
10. A. A. Zyuzin and A. Y. Zyuzin, "Flat band in disorder-driven non-Hermitian Weyl semimetals," Phys. Rev. B **97**(4), 041203 (2018).
11. L. Xiao, T. Deng, K. Wang, G. Zhu, Z. Wang, W. Yi, and P. Xue, "Non-Hermitian bulk–boundary correspondence in quantum dynamics," Nat. Phys. **16**(7), 761–766 (2020).
12. Z. Gong, Y. Ashida, K. Kawabata, K. Takasan, S. Higashikawa, and M. Ueda, "Topological phases of non-Hermitian systems," Phys. Rev. X **8**(3), 031079 (2018).
13. H.-K. Lau and A. A. Clerk, "Fundamental limits and non-reciprocal approaches in non-Hermitian quantum sensing," Nat. Commun. **9**(1), 4320 (2018).
14. H. Jiang, L.-J. Lang, C. Yang, S.-L. Zhu, and S. Chen, "Interplay of non-Hermitian skin effects and Anderson localization in nonreciprocal quasiperiodic lattices," Phys. Rev. B **100**(5), 054301 (2019).
15. T. T. Koutserimpas and R. Fleury, "Nonreciprocal gain in non-Hermitian time-Floquet systems," Phys. Rev. Lett. **120**(8), 087401 (2018).
16. A. Ghatak and T. Das, "New topological invariants in non-Hermitian systems," J. Phys.: Condens. Matter **31**(26), 263001 (2019).
17. H. Shen, B. Zhen, and L. Fu, "Topological band theory for non-Hermitian Hamiltonians," Phys. Rev. Lett. **120**(14), 146402 (2018).
18. S. Longhi, "Probing non-Hermitian skin effect and non-Bloch phase transitions," Phys. Rev. Res. **1**(2), 023013 (2019).
19. N. Okuma, K. Kawabata, K. Shiozaki, and M. Sato, "Topological origin of non-Hermitian skin effects," Phys. Rev. Lett. **124**(8), 086801 (2020).

20. L. Li, C. H. Lee, S. Mu, and J. Gong, "Critical non-Hermitian skin effect," Nat. Commun. **11**(1), 5491 (2020).
21. X. Zhu, H. Wang, S. K. Gupta, H. Zhang, B. Xie, M. Lu, and Y. Chen, "Photonic non-Hermitian skin effect and non-Bloch bulk-boundary correspondence," Phys. Rev. Res. **2**(1), 013280 (2020).
22. K. Zhang, Z. Yang, and C. Fang, "Universal non-hermitian skin effect in two and higher dimensions," Nat. Commun. **13**(1), 2496 (2022).
23. S. Longhi, "Non-Hermitian gauged topological laser arrays," Ann. Phys. **530**(7), 1800023 (2018).
24. M. H. Teimourpour, L. Ge, D. N. Christodoulides, and R. El-Ganainy, "Non-Hermitian engineering of single mode two dimensional laser arrays," Sci. Rep. **6**(1), 33253 (2016).
25. B. Zhu, Q. Wang, D. Leykam, H. Xue, Q. J. Wang, and Y. Chong, "Anomalous single-mode lasing induced by nonlinearity and the non-Hermitian skin effect," Phys. Rev. Lett. **129**(1), 013903 (2022).
26. M. De Carlo, F. De Leonardis, R. A. Soref, L. Colatorti, and V. Passaro, "Non-Hermitian sensing in photonics and electronics: A review," Sensors **22**(11), 3977 (2022).
27. M. P. Hokmabadi, A. Schumer, D. N. Christodoulides, and M. Khajavikhan, "Non-Hermitian ring laser gyroscopes with enhanced Sagnac sensitivity," Nature **576**(7785), 70–74 (2019).
28. J. C. Budich and E. J. Bergholtz, "Non-Hermitian topological sensors," Phys. Rev. Lett. **125**(18), 180403 (2020).
29. Y. Ao, X. Hu, Y. You, C. Lu, Y. Fu, X. Wang, and Q. Gong, "Topological phase transition in the non-Hermitian coupled resonator array," Phys. Rev. Lett. **125**(1), 013902 (2020).
30. C. Yuce, "Spontaneous topological pumping in non-Hermitian systems," Phys. Rev. A **99**(3), 032109 (2019).
31. J. Seo, P. Roushan, H. Beidenkopf, Y. S. Hor, R. J. Cava, and A. Yazdani, "Transmission of topological surface states through surface barriers," Nature **466**(7304), 343–346 (2010).
32. S. K. Gupta, Y. Zou, X.-Y. Zhu, M.-H. Lu, L.-J. Zhang, X.-P. Liu, and Y.-F. Chen, "Parity-time symmetry in non-Hermitian complex optical media," Adv. Mater. **32**(27), 1903639 (2019).
33. K. Jones-Smith and H. Mathur, "Non-Hermitian quantum Hamiltonians with PT symmetry," Phys. Rev. A **82**(4), 042101 (2010).
34. C. Yuce and Z. Oztas, "PT symmetry protected non-Hermitian topological systems," Sci. Rep. **8**(1), 17416 (2018).
35. R. El-Ganainy, K. G. Makris, M. Khajavikhan, Z. H. Musslimani, S. Rotter, and D. N. Christodoulides, "Non-Hermitian physics and PT symmetry," Nat. Phys. **14**(1), 11–19 (2018).
36. C. Yuce, "Topological phase in a non-Hermitian PT symmetric system," Phys. Lett. A **379**(18-19), 1213–1218 (2015).
37. S. Longhi, "Non-Hermitian topological phase transition in PT-symmetric mode-locked lasers," Opt. Lett. **44**(5), 1190–1193 (2019).
38. S. Xia, D. Kaltsas, D. Song, I. Komis, J. Xu, A. Szameit, H. Buljan, K. G. Makris, and Z. Chen, "Nonlinear tuning of PT symmetry and non-Hermitian topological states," Science **372**(6537), 72–76 (2021).
39. X. Ni, D. Smirnova, A. Poddubny, D. Leykam, Y. Chong, and A. B. Khanikaev, "PT phase transitions of edge states at PT symmetric interfaces in non-Hermitian topological insulators," Phys. Rev. B **98**(16), 165129 (2018).
40. M. Klett, H. Cartarius, D. Dast, J. Main, and G. Wunner, "Relation between PT-symmetry breaking and topologically nontrivial phases in the Su-Schrieffer-Heeger and Kitaev models," Phys. Rev. A **95**(5), 053626 (2017).
41. F. Mostafavi, C. Yuce, O. S. Magan a-Loaiza, H. Schomerus, and H. Ramezani, "Robust localized zero-energy modes from locally embedded PT-symmetric defects," Phys. Rev. Res. **2**(3), 032057 (2020).
42. V. M. Alvarez, J. B. Vargas, and L. F. Torres, "Non-Hermitian robust edge states in one dimension: anomalous localization and eigenspace condensation at exceptional points," Phys. Rev. B **97**(12), 121401 (2018).
43. L. E. F. Torres, "Perspective on topological states of non-Hermitian lattices," J. Phys. Mater. **3**(1), 014002 (2020).
44. W. Song, W. Sun, C. Chen, Q. Song, S. Xiao, S. Zhu, and T. Li, "Breakup and recovery of topological zero modes in finite non-Hermitian optical lattices," Phys. Rev. Lett. **123**(16), 165701 (2019).
45. S. Weimann, M. Kremer, Y. Plotnik, Y. Lumer, S. Nolte, K. G. Makris, M. Segev, M. C. Rechtsman, and A. Szameit, "Topologically protected bound states in photonic parity–time-symmetric crystals," Nat. Mater. **16**(4), 433–438 (2017).
46. F. K. Kunst, E. Edvardsson, J. C. Budich, and E. J. Bergholtz, "Biorthogonal bulk-boundary correspondence in non-Hermitian systems," Phys. Rev. Lett. **121**(2), 026808 (2018).
47. J.-W. Rhim, J. Behrends, and J. H. Bardarson, "Bulk-boundary correspondence from the intercellular Zak phase," Phys. Rev. B **95**(3), 035421 (2017).
48. C. L. Wong, J. Liu, K. T. Law, and P. A. Lee, "Majorana flat bands and unidirectional majorana edge states in gapless topological superconductors," Phys. Rev. B **88**(6), 060504 (2013).
49. F. Baboux, E. Levy, A. Lemaître, C. Gómez, E. Galopin, L. Le Gratiet, I. Sagnes, A. Amo, J. Bloch, and E. Akkermans, "Measuring topological invariants from generalized edge states in polaritonic quasicrystals," Phys. Rev. B **95**(16), 161114 (2017).
50. J. C. Avila, H. Schulz-Baldes, and C. Villegas-Blas, "Topological invariants of edge states for periodic two-dimensional models," Math. Phys. Anal. Geom. **16**(2), 137–170 (2013).
51. S. Yao and Z. Wang, "Edge states and topological invariants of non-Hermitian systems," Phys. Rev. Lett. **121**(8), 086803 (2018).
52. K. Kawabata, K. Shiozaki, M. Ueda, and M. Sato, "Symmetry and topology in non-Hermitian physics," Phys. Rev. X **9**(4), 041015 (2019).
53. Z.-D. Song, L. Elcoro, and B. A. Bernevig, "Twisted bulk-boundary correspondence of fragile topology," Science **367**(6479), 794–797 (2020).

54. R. Koch and J. C. Budich, "Bulk-boundary correspondence in non-Hermitian systems: stability analysis for generalized boundary conditions," Eur. Phys. J. D **74**(4), 70 (2020).
55. Y. Xiong, "Why does bulk boundary correspondence fail in some non-Hermitian topological models," J. Phys. Commun. **2**(3), 035043 (2018).
56. A. Medhi and V. B. Shenoy, "Continuum theory of edge states of topological insulators: variational principle and boundary conditions," J. Phys.: Condens. Matter **24**(35), 355001 (2012).
57. D. Cheng, B. Peng, M. Xiao, X. Chen, L. Yuan, and S. Fan, "Truncation-dependent PT phase transition for the edge states of a two-dimensional non-Hermitian system," Phys. Rev. B **105**(20), L201105 (2022).
58. J. H. Kang, J. H. Han, and Y. Shin, "Creutz ladder in a resonantly shaken 1D optical lattice," New J. Phys. **22**(1), 013023 (2020).
59. J. H. Kang, J. H. Han, and Y. Shin, "Realization of a cross-linked chiral ladder with neutral fermions in a 1D optical lattice by orbital-momentum coupling," Phys. Rev. Lett. **121**(15), 150403 (2018).
60. X. Li, E. Zhao, and W. Vincent Liu, "Topological states in a ladder-like optical lattice containing ultracold atoms in higher orbital bands," Nat. Commun. **4**(1), 1523 (2013).
61. T. Vekua, G. Japaridze, and H.-J. Mikeska, "Phase diagrams of spin ladders with ferromagnetic legs," Phys. Rev. B **67**(6), 064419 (2003).
62. M. Tsuchiizu and A. Furusaki, "Generalized two-leg hubbard ladder at half filling: phase diagram and quantum criticalities," Phys. Rev. B **66**(24), 245106 (2002).
63. M. Mancini, G. Pagano, G. Cappellini, L. Livi, M. Rider, J. Catani, C. Sias, P. Zoller, M. Inguscio, M. Dalmonte, and L. Fallani, "Observation of chiral edge states with neutral fermions in synthetic Hall ribbons," Science **349**(6255), 1510–1513 (2015).
64. M. Arikawa, S. Tanaya, I. Maruyama, and Y. Hatsugai, "Edge states of a spin-1/2 two-leg ladder with four-spin ring exchange," Phys. Rev. B **79**(20), 205107 (2009).
65. X. Yang, X. Zhang, C. Li, and Z. Song, "Dynamical signature of the moiré pattern in a non-Hermitian ladder," Phys. Rev. B **98**(8), 085306 (2018).
66. L. Li, C. H. Lee, and J. Gong, "Topological switch for non-Hermitian skin effect in cold-atom systems with loss," Phys. Rev. Lett. **124**(25), 250402 (2020).
67. M.-A. Miri and A. Alù, "Exceptional points in optics and photonics," Science **363**(6422), eaar7709 (2019).
68. I. Maruyama, T. Hirano, and Y. Hatsugai, "Topological identification of a spin-1/2 two-leg ladder with four-spin ring exchange," Phys. Rev. B **79**(11), 115107 (2009).
69. T. E. Lee, "Anomalous edge state in a non-Hermitian lattice," Phys. Rev. Lett. **116**(13), 133903 (2016).
70. K. Esaki, M. Sato, K. Hasebe, and M. Kohmoto, "Edge states and topological phases in non-Hermitian systems," Phys. Rev. B **84**(20), 205128 (2011).
71. S. Malzard and H. Schomerus, "Bulk and edge-state arcs in non-Hermitian coupled-resonator arrays," Phys. Rev. A **98**(3), 033807 (2018).
72. D. Hügel and B. Paredes, "Chiral ladders and the edges of quantum Hall insulators," Phys. Rev. A **89**(2), 023619 (2014).
73. B. Peng, Ş. K. Özdemir, F. Lei, F. Monifi, M. Gianfreda, G. L. Long, S. Fan, F. Nori, C. M. Bender, and L. Yang, "Parity–time-symmetric whispering-gallery microcavities," Nat. Phys. **10**(5), 394–398 (2014).
74. Ş. K. Özdemir, S. Rotter, F. Nori, and L. Yang, "Parity–time symmetry and exceptional points in photonics," Nat. Mater. **18**(8), 783–798 (2019).
75. D. J. Thouless, "Electrons in disordered systems and the theory of localization," Phys. Rep. **13**(3), 93–142 (1974).
76. M. A. Bandres, S. Wittek, G. Harari, M. Parto, J. Ren, M. Segev, D. N. Christodoulides, and M. Khajavikhan, "Topological insulator laser: Experiments," Science **359**(6381), eaar4005 (2018).
77. M. Parto, S. Wittek, H. Hodaei, G. Harari, M. A. Bandres, J. Ren, M. C. Rechtsman, M. Segev, D. N. Christodoulides, and M. Khajavikhan, "Edge-mode lasing in 1D topological active arrays," Phys. Rev. Lett. **120**(11), 113901 (2018).
78. H. Zhao, P. Miao, M. H. Teimourpour, S. Malzard, R. El-Ganainy, H. Schomerus, and L. Feng, "Topological hybrid silicon microlasers," Nat. Commun. **9**(1), 981 (2018).
79. J. M. Zeuner, M. C. Rechtsman, Y. Plotnik, Y. Lumer, S. Nolte, M. S. Rudner, M. Segev, and A. Szameit, "Observation of a topological transition in the bulk of a non-Hermitian system," Phys. Rev. Lett. **115**(4), 040402 (2015).
80. M. Hafezi, S. Mittal, J. Fan, A. Migdall, and J. Taylor, "Imaging topological edge states in silicon photonics," Nat. Photonics **7**(12), 1001–1005 (2013).
81. Y. Hu, M. Yu, D. Zhu, N. Sinclair, A. Shams-Ansari, L. Shao, J. Holzgrafe, E. Puma, M. Zhang, and M. Lončar, "On-chip electro-optic frequency shifters and beam splitters," Nature **599**(7886), 587–593 (2021).
82. T. Dai, Y. Ao, and J. Bao, *et al.*, "Topologically protected quantum entanglement emitters," Nat. Photonics **16**(3), 248–257 (2022).
83. Y. Hu, M. Yu, B. Buscaino, N. Sinclair, D. Zhu, R. Cheng, A. Shams-Ansari, L. Shao, M. Zhang, J. M. Kahn, and M. Lončar, "High-efficiency and broadband on-chip electro-optic frequency comb generators," Nat. Photonics **16**(10), 679–685 (2022).
84. L. Yuan, Q. Lin, M. Xiao, and S. Fan, "Synthetic dimension in photonics," Optica **5**(11), 1396–1405 (2018).
85. L. Yuan, Y. Shi, and S. Fan, "Photonic gauge potential in a system with a synthetic frequency dimension," Opt. Lett. **41**(4), 741–744 (2016).

86. K. Wang, A. Dutt, K. Y. Yang, C. C. Wojcik, J. Vučković, and S. Fan, "Generating arbitrary topological windings of a non-Hermitian band," Science **371**(6535), 1240–1245 (2021).
87. D. Yu, B. Peng, X. Chen, X.-J. Liu, and L. Yuan, "Topological holographic quench dynamics in a synthetic frequency dimension," Light: Sci. Appl. **10**(1), 209 (2021).
88. A. Balčytis, T. Ozawa, Y. Ota, S. Iwamoto, J. Maeda, and T. Baba, "Synthetic dimension band structures on a Si CMOS photonic platform," Sci. Adv. **8**(4), eabk0468 (2022).
89. G. Li, L. Wang, R. Ye, S. Liu, Y. Zheng, L. Yuan, and X. Chen, "Observation of flat-band and band transition in the synthetic space," Adv. Photonics **4**(03), 036002 (2022).
90. A. Dutt, L. Yuan, K. Y. Yang, K. Wang, S. Buddhiraju, J. Vučković, and S. Fan, "Creating boundaries along a synthetic frequency dimension," Nat. Commun. **13**(1), 3377 (2022).
91. C. Chen, X. Ding, J. Qin, Y. He, Y.-H. Luo, M.-C. Chen, C. Liu, X.-L. Wang, W.-J. Zhang, H. Li, L.-X. You, Z. Wang, D.-W. Wang, B. C. Sanders, C.-Y. Lu, and J.-W. Pan, "Observation of topologically protected edge states in a photonic two-dimensional quantum walk," Phys. Rev. Lett. **121**(10), 100502 (2018).
92. H. Chalabi, S. Barik, S. Mittal, T. E. Murphy, M. Hafezi, and E. Waks, "Synthetic gauge field for two-dimensional time-multiplexed quantum random walks," Phys. Rev. Lett. **123**(15), 150503 (2019).
93. S. Weidemann, M. Kremer, T. Helbig, T. Hofmann, A. Stegmaier, M. Greiter, R. Thomale, and A. Szameit, "Topological funneling of light," Science **368**(6488), 311–314 (2020).
94. C. Leefmans, A. Dutt, J. Williams, L. Yuan, M. Parto, F. Nori, S. Fan, and A. Marandi, "Topological dissipation in a time-multiplexed photonic resonator network," Nat. Phys. **18**(4), 442–449 (2022).